Nigerian Journal of Theoretical and Environmental Physics (NJTEP)
ISSN Online: 1597-9849
ISSN Print: 3026-9601
DOI: https://doi.org/10.62292/njtep.v3i1.2025.60
Volume 3(1), March 2025

Theoretical Investigation of Quantum Confinements in Spherical PbSrSe Semiconductor Quantum Dots

***Uwaoma, C. J., Oriaku, C. I., Nwaokorongwu, E. C. and Okwara, E. I.**

Department of Physics, College of Physical and Applied Sciences, Michael Okpara University of Agriculture, Umudike.

*Corresponding author's email: uwaomachinkata@gmail.com Phone: +2348030643221

Keywords:
Quantum,
Confinements,
Semiconductor,
PbSrSe,
Quantum Dots.

ABSTRACT

One of the IV-VI material systems that have shown promising growth and sustainability in optoelectronic applications is PbSrSe quantum dot structure (QDs) material. However, the material system belongs to the lead salt semiconductor group and has a constant energy surface with prolate ellipsoids of revolution, as well as a strongly nonparabolic energy band. In this study, the particle in a box model based on the effective mass approximation is used to theoretically investigate quantum confinement in PbSrSe spherical semiconductor quantum dots. For the first four excited states explored, it is found that the transition energies of $Pb_{0.94}Sr_{0.066}Se$ quantum dot depends on the quantum dot size.

INTRODUCTION

Semiconductor quantum dots (QDs) have arisen as a fascinating subject of study due to their unique electrical properties caused by quantum confinement. These nanoscale structures behave differently based on their size than bulk semiconductors. In this study, we concentrate on spherical PbSrSe quantum dots in order to understand the complex interplay between confinement effect, energy level, and optical features. Quantum confinement causes distinct energy states within quantum dots, resulting in a blue shift in their absorption and emission spectra (Wei, 2014). As QD size lowers, the electronic wave function becomes more confined, influencing charge carrier dynamics (Wei, 2014).

Lead salt or IV-VI material systems are desired for a variety of applications, including IR spectroscopy, low-cost mid-IR sensors, mid-IR optoelectronic devices, and medicinal applications (Khodr, 2015). According to literature reports, health problems such as breast cancer and lung cancer include biomarker molecules in exhaled breath at infrared (IR) wavelengths. Tunable Laser Spectroscopy (TLS) is a new method that has the potential to play an important role in detecting these biomarkers. The band gaps of IV-VI alloys vary from 0 to more than 500meV (0.5eV) depending on their composition and temperature. They are direct gap materials having conduction and valence band minima at the L-point in k-space (Oriaku and Khodr 2017).

Because of their size-dependent applications, QDs' optoelectronic properties have received a lot of attention in recent years. Variation in particle size causes a distinct difference in optical and electrical characteristics. PbSrSe and its alloys are among the most studied semiconductor nanoparticles due to their usefulness in a variety of applications such as optical filters and sensors, optical recording resources, and laser materials.

Improvements have been made both theoretically and empirically in researching the electrical and optical properties of IV-VI semiconductors, although many gaps remain to be addressed. For example, knowledge of quantum confinement in ternary PbSrSe QD materials that fully account for the existing anisotropy has yet to be documented. As a result, there is an imperative necessity for extensive research on these materials. Quantum confinements in spherical semiconductor QD are explored to contribute to a better understanding of the quantum characteristics of these materials and to the advancement of knowledge in concentrated matter. The work aimed to theoretically analyze quantum confinements in spherical semiconductor quantum dots.

Semiconductor Quantum Dot and Quantum Confinement

Quantum dots are semiconductors ultra-size (2-10 nm) made up of 100-10,000 atoms, we called them (artificial

atoms). These semiconductors nanocrystal with nanometer size diameter have quantum properties which can be their optical and electromagnetic effects by their quantum size effect. QDs have unique optical properties due to changes in band gap energy caused by quantum confinement effects. When light is absorbed by the quantum dots, electrons are excited from the valence band to the conduction band, leaving a hole in the valence band. When the electron and hole recombine, energy is released in the form of photo (Majeh and Khodr, 2015).

Quantum confinement is the spatial confinement of electron-hole pairs (excitons) in one or more dimensions within a material caused by the confinement of the electronic wave function to the particle's physical dimensions (Oriaku *et al.,* 2022). There are:

1D confinement: Quantum Wells
2D confinement: Quantum Wire
3D confinement: Quantum Dot

Size Quantization Effect

The quantum size effect (QSE) is a phenomena seen in nanomaterials that causes their electrical, optical, and magnetic characteristics to differ from those of the bulk material as the material's size increases. As previously stated, quantum dots are minuscule crystals containing a few hundred to a few thousand atoms and measuring on the nanometer scale. Because of their small size, the bulk materials' characteristics vary significantly (Alivisatos, 1996).

The Quantum Size Effect is caused by the confinement of electrons within nanomaterials. When the size of these materials approaches the de Broglie wavelength of electrons, it restricts their travel, resulting in discrete energy levels. The quantization of energy levels is the defining feature of QSE, and it has a significant impact on the material's physical and chemical properties.

Furthermore, the huge surface to volume ratio, in which a big fraction of a crystal's atoms are located at the surface and contribute to distinct features in the nanoscale than those of larger crystals, in which these atoms do not play a significant influence in the overall behavior of the material. Second, size influences the electrical structure in this size regime (size quantization effect), and semiconductor quantum dots, the focus of this work, are the best instructive examples for explaining this phenomena. An electron and a hole in the dot enhance the energy of the exciton as the radius r approaches the value of the exciton's Bohr radius, α_B. The band gap eventually increases as the quantum dot radius decreases. This phenomenon is known as the size quantization effect (Iyer, 2011).

Applications of Semiconductor Quantum Dots

The principal implementations of QDs are in energy efficient lighting, photovoltaics, and biological imaging.

Quantum dots solar cells

A solar cell is a device that uses quantum dots as the photovoltaic material for absorption. A solar cell is a PN junction made up of multiple layers of semiconductors, one of which is a donor (N-type) and the other an acceptor (P-type) created through the doping process. An electric field forms between these two layers, preventing electrons from moving. When incoming photons contact the cell and are absorbed by the junction, if the photon's energy is more than or equal to the semiconductor's band gap energy, it is absorbed and transferred to the electron, resulting in an electron hole pair.

These electron-hole pairs can then drift through the built-in electric field of the PN junction, contributing to the device's net current. It aims to replace bulk materials including CIGS, CdTe, and silicon (Wei, 2014). Dot Solar Quantum cells can absorb energy 24 hours a day. While the greatest technique to absorb visible light is through standard black silicone panels at daytime peak, QD Solar cells can absorb power from ultraviolet to infrared light and provide output both day and night. Third-generation solar cells include semiconductor quantum dots. This complex technique uses nanotechnology and quantum mechanics theories to improve the performance of conventional solar cells. While quantum dot solar cells have not yet been used in practice, a wide range of theoretical and experimental computations have proven their ability to meet the high conversion efficiency criteria (Nozik, 2002).

Quantum dots laser

A quantum dot laser is a semiconductor laser that employs quantum dots in its light-emitting area as an active laser medium. Load carriers in quantum spots have an electronic structure comparable to that of atoms because they are firmly bound. Lasers are made from a device that is more similar to gas lasers in such an active medium, and thus avoid some of the disadvantages of device performance related with traditional lasers based on bulk or well-active amounts. Recently, commercial applications have emerged for quantum dot active media (laser scalpel, optical coherence tomography), screen technologies (projection, laser television), spectroscopy, and telecommunications (Ahmed and Mohammed, 2010).

Using this technology, a 10 Gbit/S quantum dot laser that is unaffected by temperature changes was created for application in optical data and networks. The laser is able to run at a high-speed temperature between 20°C and 70°C, with 1.3μm wavelengths. It operates in optical, optical LANs and metro-access systems. The novel quantum dot laser outperforms previous strained quantum-well lasers in terms of temperature stability.

Quantum dots antibody

One of the main issues in biology is how cells move, interact and develop in living organisms. These questions, which have resulted in a molecular understanding of cellular events, have been responded to tremendously. QDs can be utilized to study the layout and distribution of receptors in the plasma membrane due to their intrinsic image stability. Multiplexed, phenotypic, intravial cytometric imagery requires the use of new, long-circulated conjugates which have a suitable size and are virtually non-specific to cell/serum binding while binding to highly specific cells of interest (Khodr, 2015).

Furthermore, these conjugates must be stable and have a high quantum return in the living environment. This can be achieved here using a compact quantum dot (QD)-Ab conjugate (15 nm of hydrodynamic diameter). This in vivo cytometric approach can be used in structural and functional imaging to explore interactions between cells, cells, and the environment in healthy and sick tissues (Han, 2015).

Quantum dots for cancer diagnosis

Cancer is one in every four deaths caused by cancer in Nigeria and a major public health problem in the world. Despite improvements in reducing incidence, mortality, and survival, cancer continues to kill more individuals under the age of 85 than heart disease. One of the most pressing challenges is how cancer is detected early on, when it is still treatable. New technologies are needed to improve the early detection and treatment of cancer significantly and fluorescent molecules can play a major role here. Nanotechnology is an evolving field that may have potentials to make paradigm changes in the detection, treatment, and prevention of cancer. The advancement of biocompatible nanoparticles for molecular targeted diagnosis and treatment is an area of considerable interest (Han, 2015).

Physics of PbSrSe

The lead salt IV - VI PbSe-based compounds have recently received a lot of attention due to their potential optoelectronic applications. Alloying Sr into PbSe can greatly boost its band gap energy (Xu *et al.* 2000). The wide tuning range of the energy bands within the ternary system, combined with the ease of producing good quality material with excellent homogeneity and small lattice mismatch on BaF2 substrates (Lambrecht *et al.*, 1991) and the possibility of epitaxial growth on Si substrates (Mûller *et al.*, 1997), has made PbSrSe the basis for devices operating over the wide mid-infrared wavelength range, making it particularly useful for mid-infrared intrinsic detectors and lasers. The material exhibits a multi-valley band structure, with band extrema located near the L-point of the Brillouin zone.

The absence of a heavy-hole band lowers the non-radiative Auger recombination rate by one or two orders of magnitude compared to narrow gap III-V and II-VI materials (Fang *et al.*, 2023), allowing for a drop in the high temperature threshold current. At low generation rates, stimulated emission might emerge due to lower state density and stronger interband matrix elements. Strong continuous-wave room temperature stimulated emission luminescence has been recorded between 3.0 and 4.0 mm from PbSrSe multiple quantum dot (MQD) structures, which is significantly higher than the limit of 2.3 mm in type II quantum cascade laser devices employing narrow gap III-V antimonide semiconductor materials. However, the design of optoelectronic devices in PbSrSe systems has been impeded by a lack of precise knowledge of numerous material characteristics (McCann *et al.*, 1999).

Quantum Dot as a Particle in a Box

The "Particle in a box" problem in quantum physics is difficult to visualize. This is due to the lack of a truly good example of such a system up until now. The situation has changed since the introduction of quantum dots. Small semiconductor particles are contained within the semiconductors used in microelectronics. These may contain an electron as well as a hole. It is a real-world "Particle in a Box" system; electrons will never leave the semiconductor particle. The effects of adjusting the size of quantum dots on the system's energy level are plainly seen. The simplest form of the particle in a box model takes into account a one-dimensional system. The particle can only go backwards and forwards in a straight line with impenetrable barriers at both ends. The walls of a one-dimensional box can be viewed as regions of space with indefinitely high potential energy (Majed and Khodr, 2015).

MATERIALS AND METHODS

Method of Simulation

The confinement effects of PbSrSe spherical semiconductor quantum dots were explored using a particle in a box model. The theoretical simulations were performed using the MATLAB computer program.

Numerical Calculation

The effective masses of electrons and holes, dielectric constant, binding energy, and energy gap of the constituent binary semiconductors approximated as fitting parameters required for computation were obtained from Hanada (2013).

Isotropy and Effective Masses Calculations

Lead salts are direct energy gap semiconductors with constant energy surface that are prolate ellipsoids of revolution characterizes by the longitudinal and transverse effective masses m*l and m*t, respectively.

The major axes of the ellipsoids were in the directions. To compute m*w, which was utilized to calculate the energy level of the single quantum dot system, a relationship between it and longitudinal and transverse effective mass must be discovered and applied. In Kane's two-band approximation, the energy-wave vector relationship of the conduction and valence bands of lead salt semiconductors is given by:

$$E = -\frac{1}{2}Eg \pm \sqrt{\frac{1}{4}Eg^2 + p_t^2k_t^2 + p_l^2k_l^2} \qquad (1)$$

Where the + sign is for conduction band and - sign is for the valence band. The zero energy level was taken at the bottom of the conduction band. The band gap is Eg,k_t and k_l were the transverse and longitudinal components of the wave vector and p_t^2 and p_l^2 represented the transverse and longitudinal momentum matrix element taken between the valence and conduction band states and were related to the effective masses m_l^* and m_t^* by the following relation:

$$p_{t,}^2 l = \frac{h^2 Eg}{2m_t^* l} \qquad (2)$$

where $\mu$is the exciton reduced mass defined as:

$$\mu = m_e m_h/(m_e+m_h) \qquad (3)$$

where:

$$\frac{1}{m_e} = \frac{2}{3m_e^{\perp}} + \frac{\varepsilon^{\perp}(0)}{3\varepsilon^{\parallel}(0)m_e^{\parallel}} \qquad (4)$$

$$\frac{1}{m_h} = \frac{2}{3m_h^{\perp}} + \frac{\varepsilon^{\perp}(0)}{3\varepsilon^{\parallel}(0)m_h^{\parallel}} \qquad (5)$$

$where, m_e^{\parallel}, m_e^{\perp}, m_h^{\parallel}, m_h^{\perp}$ were effective masses of electron and hole parallel and perpendicular respectively.

Dielectric constant:

The dielectric constant of the medium is defined as:

$$\mu(0) = \sqrt{\varepsilon^{\parallel}(0)\varepsilon^{\perp}(0)} \qquad (6)$$

Where:

$\mu^{\parallel}(0)\ and\ \varepsilon^{\perp}(0)$ are static dielectric parallel and perpendicular respectively.

Binding energy:

The exciton form of the Rydberg constant (i.e. the binding energy of the exciton ground state) depends on the decreased mass of the exciton. It is described as:

$$E_B = \frac{\hbar^2}{2\mu a_B^2} \qquad (7)$$

where E_B is binding energy, $\hbar^2$ is plank's constant, a_B^2 is Bohr radius.

Confinement energy:

For a spherically symmetrical potential box with an infinite barrier, the energy of the exciton can be expressed as:

$$E = E_g + \frac{\hbar^2}{8R^2}\left(\frac{1}{m_e^*} + \frac{1}{m_h^*}\right) \qquad (8)$$

Where:

Eg is the band gap of the bulk material. The positive contribution of the confinement energy was described by the second term with a $\frac{1}{R^2}$, where *h* is the Planck's constant, and $m_{e,h}$ the effective mass of the electron and the hole respectively.

Equation 8 is a direct proportionality relationship between the Eg and the effective masses for a certain material. To a first approximation, the differences in effective masses with composition (x) and temperature (T) were caused by variations in the bandgap. The energy gap of $Pb_{1-x}Sr_xSe$ system depended on temperature according to this relation (14)

$Eg(x, T) = 0.150 + 3.608x - 1.31x^2$
$+ (0.430 - 3.093x + 6.495x^2) *10^{-3}T$ (eV)
(for $0 \leq x \leq 0.276$, $0^o < T \leq 350$k) (9)

The energy aspersion relation in the *z*-direction, $E_z(k)$, using Kane's model is similar to equation (1) and is given by:

$$E_z = -\frac{1}{2}Eg \pm \sqrt{\frac{1}{4}Eg^2 + p_z^2k^2} \qquad (10)$$

where $p_z^2 = \frac{h^2 Eg}{2m_w^*}$. The energy dispersion for lead salts in the *z*-direction can thus be found by equating equations (7) and (16). This results in the following relation:

$$\frac{k^2}{m_w^*} = \frac{k_l^2}{m_l^*} + \frac{k_t^2}{m_t^*} \qquad (11)$$

The wave vectors k_l and k_t can be written in terms of *k* as:

$$k_l = kcos\theta$$
$$k_t = ksin\theta. \qquad (12)$$

Where the angle θ is between the ellipsoidal major axis and the well growth direction, also the *z*-direction. Substituting equation (11) in equation (12) yields a relation between the effective mass in the well and the longitudinal and transverse effective masses:

$$\frac{1}{m_w^*} = \frac{(cos\theta)^2}{m_l^*} + \frac{(sin\theta)^2}{m_t^*}. \qquad (13)$$

The value of the mobility effective mass m_w^* at the band extrema is calculated from the respective carrier longitudinal mass m_l^*, transverse mass m_t^*, and the angle θ. To determine this angle for a quantum well in the [100] direction, the dot product is taken between [100] direction and the [111] ellipsoidal direction:

$[100][111]=1=\sqrt{3}cos\theta.$

Thus,

$$cos\theta = \frac{1}{\sqrt{3}}\ and\ sin\theta = \frac{2}{\sqrt{3}}$$

Now equation (12) gives the effective mass in the [100] direction as [14]:

$$\frac{1}{m_w^*} = \frac{1}{3}\left[\frac{2}{m_t^*} + \frac{1}{m_l^*}\right] = \frac{1}{m_{100}^*}. \qquad (14)$$

This value for the effective mass is in the direction of the well, not in the direction of the ellipsoid major axis [111]. To determine this angle for a quantum well in the [11-1] direction, the dot product is taken between the [11-1] direction and the [111] ellipsoid direction:

$[11\text{-}1][1111] = 1 = 3cos\theta.$

Thus, $cos\theta = \frac{1}{3}\ and\ sin\theta = \frac{2\sqrt{2}}{3}$

Now equation (12) gives the effective mass in the [111] direction as

$$\frac{1}{m_w^*} = \frac{1}{9}\left[\frac{8}{m_t^*} + \frac{l}{m_l^*}\right] = \frac{1}{m_{111}^*}. \quad (15)$$

This value for the effective mass is in the direction of the well, not in the direction of the ellipsoid major axis [111].

Interpolation Scheme

The formula of linear interpolation was used to determine the anisotropic parameters parallel (perpendicular) ||, ⊥ of the ternary material under study by using the macroscopic parameters of the end-member binary crystals. Parameters such as: mass of electron m_e, mass of hole m_h, dielectric constant ε_0, and band-gap energy E_g were determined by using the macroscopic parameters of the end-member binary materials. The formula of linear interpolation was given as:

$$(A_xB_1 - \tfrac{1}{x}C) = x(AC)_{||\perp} + (1-x)(BC)_{||\perp} \quad (16)$$

Where (AC)||(⊥) and (BC)||(⊥) are respectively, various parameters parallel and perpendicular for AC and BC binary compounds.

for the bandgap energy E_g, the following approximate relation is approved:

$$Eg_{(AxB_{1-x}C)}(x) = xEg(AC) + 1 - x)Eg(BC) - bx(1-x) \quad (17)$$

Where b is called the bowing parameter.

Temperature dependence of the bandgap energy can be expressed by the Varshni formula (Hanada, 2013)

$$E_g(T) = E_g(0) - \frac{\alpha T^2}{T+\beta} \quad (18)$$

where $E_g(T)$ is bandgap at varying temperature, $E_g(0)$ is bandgap at zero temperature, T is temperature, α and β are Varshni parameters.

RESULTS AND DISCUSSION

In this study, we first computed the effective masses in the normal and oblique valleys, then used these values to determine the transition energy state and the emitted wavelength energy state, and lastly compared our results to the experimental data given in Figure 1. We utilize this widely accepted linear equation to calculate the longitudinal effective mass of electrons, which is the same as the electron effective mass in the normal valley. This finding is in line with the work of Khodr (2017), who adopted similar method of discussion

$$m_{l,e}(x,T) = \frac{m_{l,e}(x,77k)}{Eg(x,77k)} * Eg(x,T). \quad (19)$$

A similar relationship can be used to calculate the longitudinal effective mass of the holes, which is the same as their effective mass in the normal valley. The transverse effective mass of electrons and holes may be calculated using equation (19), and by replacing the appropriate symbol from these effective values, we can apply equation (15) to obtain the effective masses in the oblique valleys (Zhong *et al.*, 2016)

Table 1 shows the calculated effective mass for the electrons and holes in both valleys for the dot material Pbse similarly the calculating effective masses for the barrier material $Pb_{0.934}$ $Sr_{0.066}Se$ can be seen in Table 2. The values are shown calculated at five different temperatures 77K, 150K, 200K, 250K and 300K. The normal valley electron and hole masses completely match the longitudinal effective masses. These findings tally with the findings of Khodr (2017), who carried out similar research titled calculations of the effective masses and emitted wavelengths of PbSe/PbSrSe quantum well normal and oblique degenerative valleys.

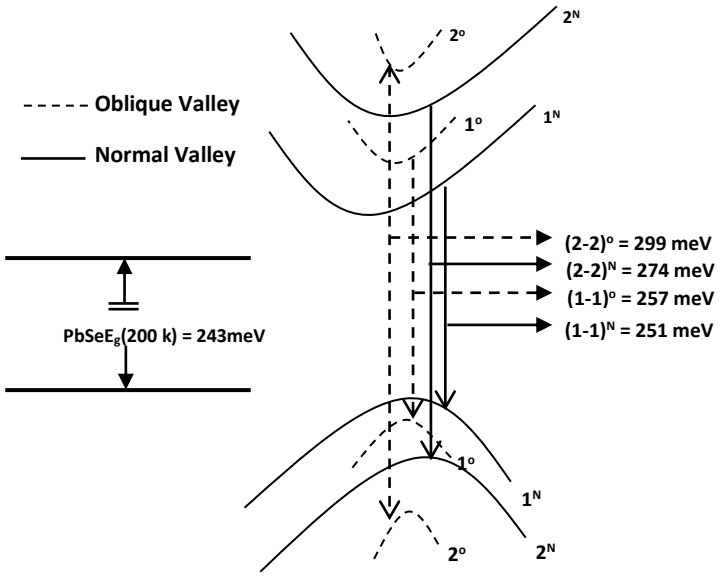

Figure 1: Illustration of interband transitions between degeneracy split *n*=1 and *n* = 2 subbands with computed energies for a 30nm wide PbSe QD at 200k

Table 1: The normal and oblique valleys effective mass calculations for PbSe dot material

T (PbSe)	Eg (*x,T)*	*ml, e*	*mt, e*	*ml, h*	*mt, h*	*meN*	*mhN*	*meo*	*Mho*
77	0.18311	0.0788	0.0475	0.0764	0.0386	0.0788	0.0764	0.046993	0.040845
150	0.2145	0.092308	0.055643	0.089497	0.045217	0.092308	0.089497	0.058212	0.047847
200	0.236	0.101561	0.06122	0.098468	0.049749	0.101561	0.098468	0.064047	0.052643
250	0.2575	0.110813	0.066797	0.0107438	0.054282	0.110813	0.107438	0.069881	0.057439
300	0.279	0.120066	0.072375	0.116409	0.058814	0.120066	0.116409	0.075716	0.062235

Table 2:The Normal and Oblique Valleys Effective Mass Calculations for PbSrSe Barrier Material

T (PbSrSe)	Eg (*x,T)*	*ml, e*	*mt, e*	*ml, h*	*mt, h*	*meN*	*mhN*	*meo*	*Mho*
77	0.401974	0.0788	0.0475	0.0764	0.0386	0.0788	0.0764	0.046993	0.040845
150	0.420527	0.082437	0.049692	0.079926	0.040382	0.082437	0.079926	0.51987	0.042731
200	0.433235	0.084928	0.051194	0.082345	0.041602	0.084928	0.082342	0.053558	0.044022
250	0.445943	0.087419	0.052696	0.084757	0.042822	0.087419	0.084757	0.055129	0.045313
300	0.45865	0.08991	0.054197	0.087172	0.044042	0.08991	0.087172	0.0567	0.046604

The first four energy levels, both parabolic and non-parabolic, were calculated, but only the first two were compared to the experimental results shown in Figure 1. In addition, the emitted wavelength was computed for each of the four energy levels and compared to experimental data. Tables 3 and 4 show the normal value calculations for a single quantum dot with radius 10nm and 100nm at 300k. The actual and theoretical values are nearly matched, with minor differences that could be related to the experimental setup or the original effective mass value employed in the computation (Geo *et al.*, 1996; Heiner, 2023; Ikeri *et al.*, 2024).

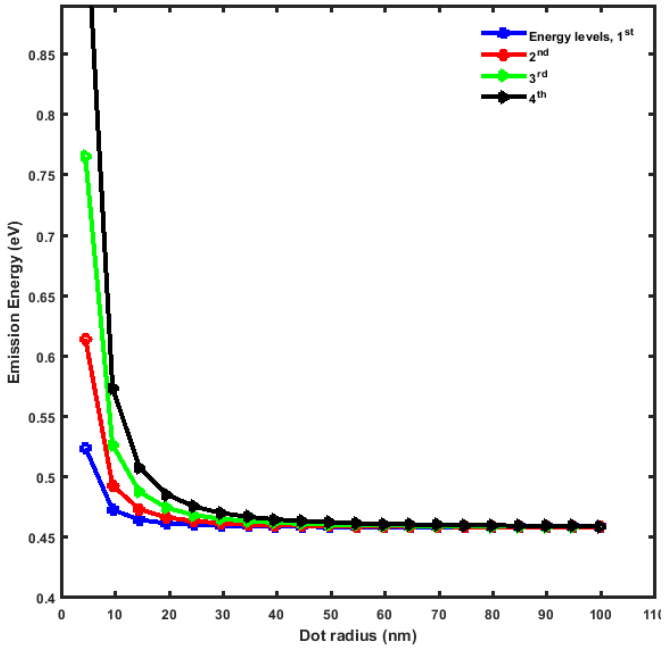

Figure 2: Plot of Transition Energy Versus Quantum Radius of $Pb_{0.94}Sr_{0.066}Se$ Quantum Dot for the 1st, 2nd, 3rd and 4th Energy States

Table 3: The Transition Energy Levels emitted Wavelengths from $Pb_{0.94}Sr_{0.066}Se$ Quantum Dot of radius R=10nm at temperature, 300K

Energy State	**Transition Energy**	
	E(eV)	**$\lambda(\mu m)$**
1st	0.4720	2.6273
2nd	0.4903	2.5292
3rd	0.5208	2.3811
4th	0.5635	2.2007

Table 4: The Transition Energy Levels emitted Wavelengths from $Pb_{0.94}Sr_{0.066}Se$ Quantum Dot of Radius R=100nm at Temperature, 300K

Energy State	Transition Energy	
	E(eV)	$\lambda(\mu m)$
1st	0.4588	2.7028
2nd	0.4590	2.7017
3rd	0.4593	2.6999
4th	0.4597	2.6974

CONCLUSION

In this study, the effective electron and hole masses in the normal and oblique valleys of a PbSeSr single quantum dot laser were calculated. These numbers were used to construct the system's first four energy levels, accounting for the bands' non-parabolicity. The theoretically values for the emitted wavelengths were verified with the experimental values, and hence we conclude that the theoretical model used and determined effective masses can predict accurate results. To further validate the accuracy of the result in this work, experimental investigation should be conducted on the theoretically studied semiconductor quantum dot material.

REFERENCES

Ahmed, S. and Mohammed, S. (2010). Electronic structure of InN/GaN quantum dots: Multimillion-atom tight-binding simulations. *IEEE Transactions on Electron Devices,"* 57(1):164-173.

Alivisatos, R.C. (1996). Electrons in Artificial atoms. *Nature*, 379(6564): p.413-419.

Fang, X. M., Philippopoulos, P., Culcer, D., Coish, W. A. and Chesi, S. (2023). Recent advances in hole-spin qubits. *Mater. Quantum Technol.*, 3 (2023) 012003, 1-28

Guo, Q., Ong, C. K., Poon, H. C. & Feng, Y. P. (1996). Calculation of electron effective masses in AlAs. *Basic Solid State Physics*, 197(1): 111-117. https://doi.org/10.1002/pssb.2221970117

Han, H. S. (2015). Quantum dot/Antibody conjugates for in Vivo Cytometric Imaging in mice. *Proceedings of the National Academy of Sciences*, 112(5): 1350-1355.

Hanada, T. (2013). Basic Properties of ZnO, GaN, and Related Materials. *Journal of Applied Physics*, 2(3), 1-19.

Heiner, L. (2023). *Quantum dots – Seeds of Nanoscience*. The Royal Swedish Academy of Sciences.

Ikeri, H. I., Tarry, S. T., Achuka, E. I., Eze, C. N., Asielu, O. K. & Ndubueze, N. D. (2024). Optical properties of PbSe, PbS, and PbTe semiconductor quantum dots and their applications. *SSRG International Journal of Material Science and Engineering*, 10(2): 19-23. http://creativecommons.org/licenses/by-nc-nd/4.0/

Iyer, G. and Shimon W. (2011). Single-Step Conjugation of Antibodies to Quantum Dots for P Labeling Cell Surface Receptors in Mammalian Cells. *Methods Mol. Biol.*, 751: 553-563.

Khodr, M. (2017). Calculations of the effective masses and emitted wavelengths of PbSe/PbSrSe quantum well normal and oblique degenerative valleys. *Far East Journal of Electronics and Communications*, 17(3): 651-660. http://dx.doi.org/10.17654/EC017030651

Khodr, M. F. and McCann, J. F. (2014). Theoretical Analysis and Design of PbSe/PbSrSe Quantum well structures of Fabricating Tunable Mid-infrared laser. *International Journal of Applied Engineering Research*, 9(17), 40-65.

Lambrecht, A., Herres, N., Spanger, B., Kuhn, K., Böttner, H., Tacke, M. and Evers, J. (1991). Molecular beam epitaxy of $Pb_{1-x}Sr_xSe$ for the use in IR devices. *Journal of Crystal Growth*, 108(1-2), 301-308

Majed, F. and Khodr, M. F. (2015). SQW PbSe/PbSrSe emitted wavelength calculations for breath analysis applications. *International Journal of Applied Engineering Research*, 10(24), 0973-456.

McCann, P. J., Namjou, K. and Fang, X. M. (1999). Above-room-temperature continuous-wave mid-infrared photoluminescence from PbSe/PbSrSe quantum wells. APPL. PHYS. LETT. 75, 3608–3610.

Müller, P., Zogg, H., Fach, A., John, J., Paglino, C., Tiwari, A.N., Krejci, M. and Kostorz, G. (1997). Reduction of Threading Dislocation Densities in Heavily Lattice Mismatched PbSe on Si(111) by Glide. *Phys. Rev. Lett. 78, 3007*. https://doi.org/10.1103/PhysRevLett.78.3007

Nozik, A. J. (2002). Quantum dot solar cells. *Physica E: Low dimensional Systems and Nanostructures*, 14(1): 115-120.

Oriaku, C. I. and Khodr, M., (2017). Calculation of the effective masses and emitted wavelengths of PbSe/PbSrSe quantum well normal and oblique degenerate valleys. *East Journal of Electronic and Communications*, 17(3).

Oriaku, C. I., Noor A., Maryam E. and Wala A., (2022). Introduction to quantum dots definition and applications. The University of Jordan.

Wei, W., (2014). Two intermediate bands solar cells of InGaN/InN quantum dot supercrystals. *Appl. Phys. A*, 116(3):1009-1016.

Zhong, S., Wu, M. & Lei, X. (2016). First-principle calculations of effective mass of silicon crystal with vacancy defects. *Materials Science-Poland*, 34(4): 916-923. https://doi.org/10.1515/msp-2016-0128